




Article

The Impact of Synthesis Method on the Properties and CO₂ Sorption Capacity of UiO-66(Ce)

Michalina Stawowy¹, Maciej Rózewicz¹, Ewa Szczepańska^{1,2}, Joaquin Silvestre-Albero³ , Mirosław Zawadzki⁴, Marta Musioł⁵, Rafał Łuzny¹ , Jan Kaczmarczyk¹, Janusz Trawczyński¹  and Agata Łamacz^{1,*}

¹ Division of Chemistry and Technology of Fuels, Wrocław University of Technology, Gdanska 7/9, 50-344 Wrocław, Poland; michalina.stawowy@pwr.edu.pl (M.S.); maciej.rozewicz@gmail.com (M.R.); ewa.szczepanska@upwr.edu.pl (E.S.); rafal.luzny@pwr.edu.pl (R.Ł.); jan.kaczmarczyk@pwr.edu.pl (J.K.); janusz.trawczynski@pwr.edu.pl (J.T.)

² Department of Chemistry, Wrocław University of Environmental and Life Sciences, 50-375 Wrocław, Poland

³ Laboratorio de Materiales Avanzados, Departamento de Química Inorgánica, Universidad de Alicante, Ctra. San Vicente-Alicante s/n, E-03690 Alicante, Spain; joaquin.silvestre@ua.es

⁴ Institute of Low Temperature and Structure Research, Polish Academy of Sciences, Okólna 2, 50-422 Wrocław, Poland; m.zawadzki@int.pan.wroc.pl

⁵ Centre of Polymer and Carbon Materials, Polish Academy of Sciences, M. Curie-Skłodowskiej 34, 41-819 Zabrze, Poland; atramsum@gmail.com

* Correspondence: agata.lamacz@pwr.edu.pl; Tel.: +48-(71)-320-65-92

Received: 28 February 2019; Accepted: 26 March 2019; Published: 29 March 2019



Abstract: A series of cerium-based UiO-66 was obtained via hydrothermal and sonochemical methods, using the same quantities of reagents (cerium ammonium nitrate (CAN), terephthalic acid (H₂BDC)) and solvents) in each synthesis. The impact of synthesis method and metal to linker ratio on the structural and textural properties of obtained UiO-66(Ce), as well as their composition in terms of Ce⁴⁺/Ce³⁺ ratio, structure defects resulting from missing linker, and CO₂ adsorption capacity was discussed. By using typical characterization techniques and methods, such as XRD, N₂ and CO₂ sorption, TGA, XPS, and SEM, it was shown that the agitation of reacting mixture during synthesis (caused by stirring or ultrasounds) allows to obtain structures that have more developed surfaces and fewer linker defects than when MOF was obtained in static conditions. The specific surface area was found to be of minor importance in the context of CO₂ adsorption than the contribution of Ce³⁺ ions that were associated with the concentration of linker defects.

Keywords: UiO-66; cerium; CO₂ sorption; sonochemical synthesis

1. Introduction

Gas adsorption and separation [1], gas storage [2], chemical sensing [3], drug delivery [4] and heterogeneous catalysis [5] are the most popular fields of metal-organic framework (MOFs) utilization. Among all classified MOF structures (over 60,000 reported in Cambridge Crystallographic Data Centre, but many of them are repeated), there are some that attract special attention owing to very high—if not outstanding—surface area, chemical properties or thermal and chemical resistance. The structure instability upon heating or in the presence of acids/bases is the main reason for hindering MOFs application in many catalytic processes. One well-recognized, stable metal-organic structure is UiO-66 that is built from hexanuclear zirconium clusters connected with 1,4-benzenedicarboxylate (H₂BDC). The UiO-66 was first reported by Cavka et al. [6]. It is characterized by good thermal and chemical stability, thanks to strong Zr-O bonds. Moreover, the UiO-66 structure exhibits excellent stability in water [7] and promising features for CO₂/CH₄ gas separation [8]. By changing metal in the node or

introducing/substituting the functional group in an organic linker, one can change the properties of the parent MOF. Modifications in UiO-66 usually affect linker, which often improves its adsorptive properties but also reduces its thermal resistance [9]. The exchange of Zr to other metals, like Hf [10] and Ti [11], has been reported, while introducing Ce⁴⁺ to an MOF structure is a promising way to obtain redox-active materials [12–15].

Nouar et al. [16] reported that partial substitution of Zr by Ce in UiO-66 enhanced binding of methanol and led to its catalytic decomposition to CO₂ which may be due to the combination of structural defects and redox activity. The authors found that cerium occurred in two oxidation states: Ce (IV) (predominantly) and Ce (III). Also, Dalapati et al. [14] detected by XPS both Ce (IV) and Ce (III) ions in UiO-66 type Ce-based MOF synthesized from cerium (IV) nitrate and 3,4-dimethylthieno [2-b] thiophene-2,5-dicarboxylic acid (H₂DMTDC). They used cerium-based MOF in the oxidation of thiophenol to 1,2-diphenyldisulfide and found that it revealed excellent oxidase-like catalytic properties, thanks to the existence of redox-active cerium atoms in the framework. In contrary, Lammert et al. [12] characterized obtained in their laboratory UiO-66(Ce) by XANES and did not detect any traces of Ce³⁺. That material was tested as co-catalyst in aerobic oxidation of benzyl alcohol, and provided significantly higher alcohol conversion than zirconium based UiO-66 or CeO₂. The Ce⁴⁺ cations in the hexanuclear cluster in MOF can catalyze redox reactions through reduction to Ce³⁺ [15]. Cerium (IV) ammonium nitrate (CAN), which is often used as a Ce precursor for UiO-66 based metal-organic frameworks, can act as a homogeneous catalyst in oxidation of alcohols, thioethers, epoxides, alkylbenzenes, and active methylene compounds [17].

Owing to its unique properties (high oxygen mobility, easy and reversible Ce⁴⁺ ↔ Ce³⁺ transition), cerium (IV) oxide has attracted significant interest in a wide range of reactions [18–20], including CO₂ conversion [21,22]. Oxygen vacancies in CeO₂ act as sites for activation of adsorbing CO₂ molecules. In general, the presence of Ce³⁺ (Lewis base) enhances CO₂ adsorption and conversion, promotes CO₂ disproportionation, and stabilizes CO-containing intermediates [21,23]. The global importance of CO₂ in terms of greenhouse gas emissions from fossil fuel-based power generators drives the need for developing new materials that can be used for its adsorption, storage, and/or conversion. Carbon dioxide is a thermodynamically stable compound with very low reactivity. Utilization of CO₂ is considered challenging because its activation requires overcoming a thermodynamic barrier. One of many possibilities of CO₂ utilization is its conversion to methanol, which is a popular solvent and key substrate in the chemical industry, e.g., for the synthesis of liquid fuels [24]. Hydrogenation of CO₂ to methanol is favored at low temperatures and high pressure. The most popular catalyst for this reaction is Cu/ZnO (also supported and/or promoted) [25]. It was reported that CeO₂-containing catalysts exhibit much-higher methanol yield in comparison with those without CeO₂ [26,27].

The issue of UiO-66 doping with cerium to obtain mono- or bimetallic MOFs that may reveal better catalytic properties than parent, Zr-based MOFs, is still to be addressed, both in the context of the improvement of particular properties of these materials (such as textural, thermal, presence of structure defects, structure homogeneity) and their redox activity. Excellent performance of ceria in CO₂ activation justifies the choice of cerium-based MOFs as potential catalysts for CO₂ conversion. It is also essential to study the surface of MOF, since structures with open metal sites characterize better CO₂ adsorption capacity [28].

Among various possibilities of MOFs preparation, i.e., solvothermal (hydrothermal when carried out in aqueous solutions), sonochemical, mechanochemical, electrochemical or microwave assisted [29], the most popular is the first one. The synthesis method, as well as its parameters, such as temperature, duration time, the type of used metal salt or solvent, the pH of the solution, may influence the properties of the final product.

In this work, we study the influence of the synthesis method on the properties of cerium-based UiO-66. The material was obtained in three different ways by using hydrothermal and sonochemical syntheses. The UiO-66(Zr) is typically obtained via solvothermal route, but a very good outcome of the sonochemical synthesis was reported by Kim et al. [30]. The use of ultrasounds during MOF

preparation allows accelerated nucleation; hence, at low reaction temperature and ambient pressure, crystallization time is short. Moreover, obtained particles are more uniform and smaller than in the case of solvothermal synthesis [31]. To our best knowledge, UiO-66(Ce) has not been obtained yet via the sonochemical route. According to recently published [12–14,32], cerium-based UiO-66 structures were obtained only by solvothermal synthesis.

2. Results and Discussion

2.1. Crystallographic structure of UiO-66(Ce) materials

The XRD patterns of UiO-66(Ce) are presented in Figure 1. It has been proven that all of the synthesized materials are crystalline and are similar to the XRD patterns of UiO-66(Zr) [33] and UiO-66(Ce), as reported in the literature [13,14]. The XRD patterns exhibit sharp reflexes around 2θ of 7.2° , 8.3° , 11.7° , 13.8° , 14.4° corresponding to reflections for the (111), (200), (220), (311) and (222) planes, respectively. All of these reflexes are somewhat shifted towards lower 2θ values compared to the UiO-66(Zr) [6], which is due to higher radii of Ce^{4+} (0.97 Å) than Zr^{4+} (0.84 Å) [34]. All of the presented diffractograms are typical for metal-organic structures. However, the diffractogram of UiO-66(Ce) obtained under continuous mixing and excess of the metal precursor (sample M (2:1)), displays intensive reflexions at 16.5° , 28.9° and 33.5° , that can be ascribed to cerium formate ($\text{Ce}(\text{HCOO})_3$), which is formed as a result of deprotonation of carboxylic acid. Significant amounts of cerium formate in the M (2:1) sample affects the textural properties and CO_2 sorption, as discussed in the next section. Besides, the difference between M (2:1) and other samples was visible during the filtering-off step. The M (2:1) sample contained two fractions—white microcrystalline powder, which was cerium formate, and yellow powder which was UiO-66(Ce). It seems that unlike other methods, the hydrothermal one with mixing is sensitive to metal: linker ratio, which results in a homogeneous product only at equimolar M:L. Moreover, the sonochemical syntheses yielded the most homogeneous product, which could be due to lower temperatures applied (50°C) and good mass transport provided by the ultrasounds. Crystallization of cerium formate is facilitated at higher temperatures and according to [35] occurs when synthesis is carried out for longer than two hours. Formation of $\text{Ce}(\text{HCOO})_3$ is a consequence of DMF hydrolysis to formic acid and dimethyl amine. That reaction is impossible to avoid in the presence of water, which was used as one of the solvents in this work. As was calculated [36], hydrogen bonds between water and amides are stronger than water molecules. The rate of DMF hydrolysis increases with temperature; therefore, the risk of cerium formate crystallization was higher during hydrothermal syntheses of UiO-66(Ce), than during sonochemical procedure. Superior formation of cerium formate during synthesis of M (2:1) was probably caused by the simultaneous occurrence of three factors: the presence of H_2O , the excess of Ce precursor and the fleeting overheating of solution, which is often a more or less serious concern when a magnetic stirrer is used. Overheating was not an issue in the case of synthesis of M (1:1), which was $\text{Ce}(\text{HCOO})_3$ -free, simply because cerium precursor was not in excess (as in the case of M(2:1)).

The crystallite sizes calculated from Scherrer equation for the [111] plane were as follows: 128 nm for UiO-66, 83.5 and 83.7 nm for H(1:1) and H(2:1); 65.8 and 59.7 nm for M(1:1) and M(2:1) and 43.4 and 46.9 nm for S(1:1) and S(2:1), respectively. Therefore, the synthesis method had an impact on the size of UiO-66(Ce) crystallites, yielding the biggest when carried out hydrothermally in static conditions (H). Smaller crystals were obtained when mixing was applied during hydrothermal synthesis (M), whereas the employment of ultrasounds (S) led to the smallest crystals.

In solution, crystals grow from molecules that must be transported from the bulk of the solution to the interface between the crystal and the solution. Therefore, mass transport is a key factor in crystal growth. Depending on the crystallization technique, the effectiveness of mass transfer is different because in each method, supersaturation is attained in a unique way. Hence, the applied procedure may affect the final product. For example, crystallization from motionless solution should lead to bigger crystals since the molecules from solution have more chances to fit already-existing crystals,

making them bigger, whereas agitation may cause molecules from the solution to hit the crystals, smashing off some molecules, so the crystals get smaller. Thus, the type of agitation affects the motion in solution; and therefore, the effectiveness of mass transfer. The rate of agitation, besides other factors such as temperature, or trace impurities, influences the rate of nucleation and the rate of crystal growth [37,38]. It can be observed in the presented study that motion of cerium precursor and linker molecules in the solution during syntheses M and S led to UiO-66(Ce) crystallites of decreased size compared to stationary conditions (H). In our case, bigger crystals were obtained when agitation was caused by stirring (M) than by ultrasounds (S). When the liquid is subjected to acoustic cavitation caused by ultrasounds, the microscopic bubbles are set into radial oscillation. They collapse very quickly, within several nanoseconds and the phenomenon repeats for a high number of bubbles in each acoustic period. Since there is possibly no mechanical equilibrium under these conditions at the microscopic scale in the liquid, local supersaturation may occur and result in more numerous, small crystals that nucleate more rapidly. The time of nucleation is the time required for the clusters to reach critical size. It can be reduced by any microscopic effect that enhances the formation of the smallest clusters. In addition, nucleation can be enhanced by segregation that is driven by cavitation bubbles [39]. It was reported by Enomoto et al. [40] that crystallization under ultrasounds from less concentrated solutions leads to smaller and more uniform particles than when the process is carried out under stirring, whereas there is no significant difference in particle size distribution between those two methods for solutions of high concentrations.

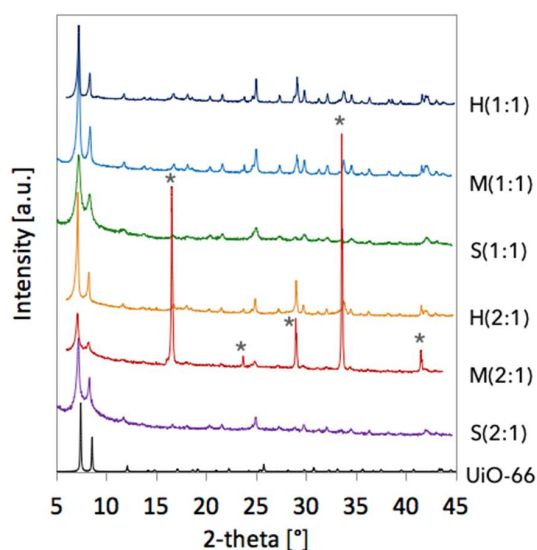


Figure 1. XRD patterns of UiO-66 and that of UiO-66(Ce) obtained in this work. The “*” is $\text{Ce}(\text{HCOO})_3$.

The crystallographic data of UiO-66(Ce) samples determined from XRD patterns are set in Table 1. The lattice parameters for all samples are similar to those reported in [13,14] and are slightly higher than calculated for UiO-66(Zr), which arises from higher ionic radii of Ce^{4+} than Zr^{4+} . It can also be observed that unit cell parameters of UiO-66(Ce) samples differ from each other, which can be due to structure defects, such as vacancies, interstitial atoms, substitutional atoms, local structure transformations, etc. The defects may cause strains in the crystal lattice of UiO-66(Ce) resulting from planar stress—either compressive (corresponding to the increase of unit cell and a peak shift to lower 2θ angles) or tensile (decrease of the unit cell, peak shift to higher 2θ angles). The strain in crystal lattice of UiO-66(Ce) samples can be caused by structure defects, such as linker or metal cluster vacancies. Whereas the occurrence and concentration of those vacancies can be affected by the method of synthesis. Moreover, the occurrence of tensile stress, and thus the decrease of unit cell parameters can be caused by the presence of Ce^{3+} ions that have bigger radius than Ce^{4+} (1.143 Å against 0.97 Å [34]). In the case of studied in this work UiO-66(Ce) obtained at M:L=1:1, the following

increase of unit cell size is observed: $H < M < S$, and it corresponds to the decrease in Ce^{3+} contribution (determined by XPS), being 47.9, 46.1 and 45.1%, respectively. For the samples obtained at the excess of metal precursor (M:L=2:1), the impact of Ce^{3+} contribution was less significant than the impact of such structural defects as linker vacancies that caused compressive stress in the lattice, thus increasing the size of the unit cell. The issues of the presence of Ce^{3+} cations and linker vacancies in the UiO-66(Ce) samples are discussed further in this paper.

Table 1. Crystallographic data of the obtained UiO-66(Ce).

Sample	a [Å]	Volume [Å ³]	D ₁₁₁ [nm]
H(1:1)	21.0469	9323.2	83.5
M(1:1)	21.2110	9543.0	65.8
S(1:1)	21.2797	9636.0	43.4
H(2:1)	21.4095	9813.4	83.7
M(2:1)	21.4544	9875.4	59.7
S(2:1)	21.3468	9727.4	46.9
UiO-66 [6]	20.7004	8870.3	-
UiO-66(Ce) [12]	21.4727	9900.6	-

Formula: $[Ce_6O_4(OH)_4(BDC)_6]$
Space group: $Fm\bar{3}m$

The XRD analyses suggest that, as reported in [6,10,12], the UiO-66(Ce) materials obtained in this work possess a face-centered cubic (fcc) framework structure and crystallize in the $Fm\bar{3}m$ space group. According to detailed studies performed by others [13,14], these materials consist of hexanuclear $[Ce_6O_4(OH)_4]^{12+}$ building blocks that are connected by the carboxylate groups of twelve BDC ligands. The framework contains two types of polyhedral cages: tetrahedral (smaller) and octahedral (larger). Each central octahedral cage is connected with eight tetrahedral cages through narrow triangular windows [14]. The topologies and structures corresponding to UiO-66(Ce) materials obtained in this work are presented in Figure 2.

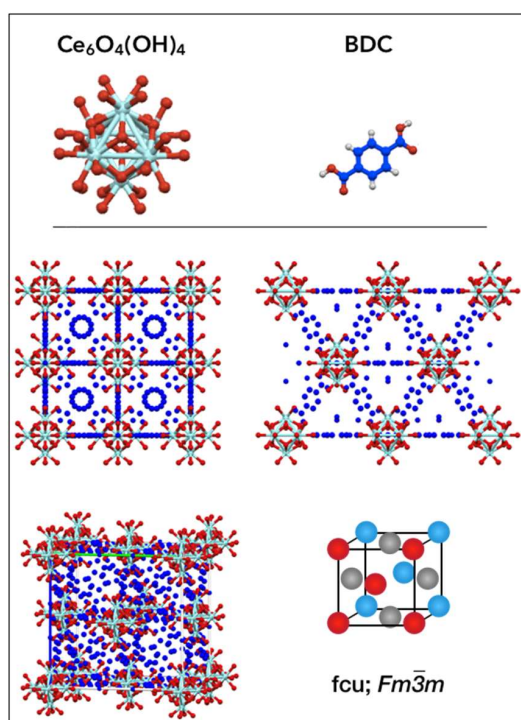


Figure 2. Topology and structure of UiO-66(Ce) materials.

The SEM pictures of M (1:1) and M (2:1) samples are shown in Figure 3. It can be seen that both contain small crystals of UiO-66(Ce), but the sample obtained at the equimolar metal to linker ratio is homogeneous (Figure 3a), while the one obtained with the excess of CAN also contains big rods of cerium formate (Figure 3b), whose presence was also confirmed by XRD.

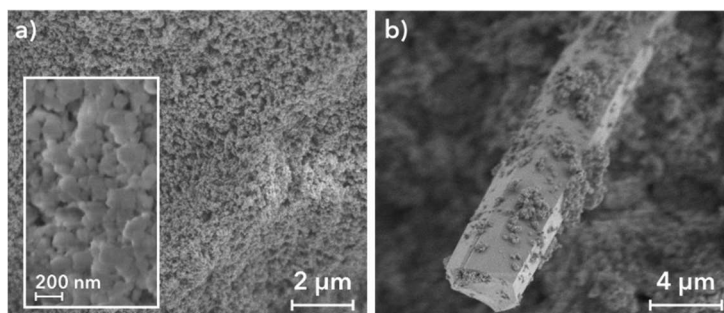


Figure 3. SEM pictures of M(1:1) (a) and M(2:1) (b) samples.

2.2. Textural properties of UiO-66(Ce)

The experiments of adsorption-desorption of N₂ (at 77K), CO₂ and benzene (both at 298 K) were conducted in order to determine the specific surface areas of obtained materials and to evaluate their porosity. Results are presented in Table 2, Figures 4 and 5.

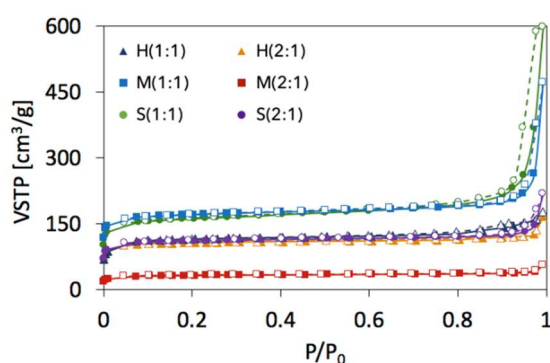


Figure 4. N₂ adsorption-desorption isotherms at 77K for UiO-66(Ce) materials (adsorption—filled symbols; desorption—empty symbols).

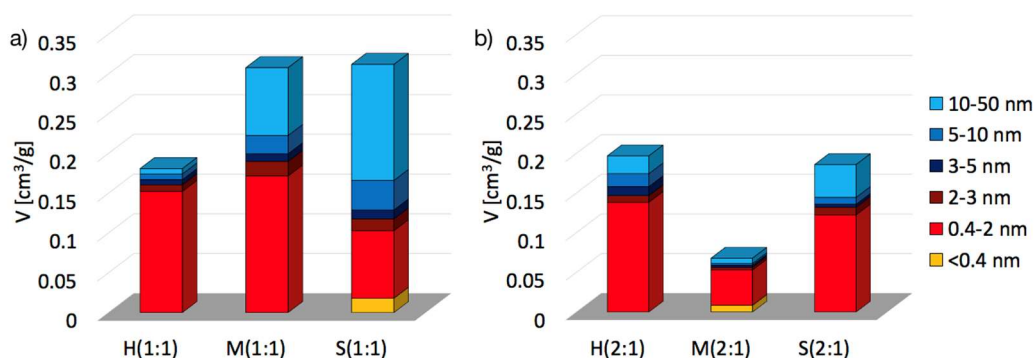


Figure 5. Distribution of the volume of sub-micropores (<0.4–2 nm), micropores (0.4–2 nm) and mesopores (2–50 nm) in UiO-66(Ce) obtained at M:L=1:1 (a) and M:L=2:1 (b).

As is shown in Table 2, the highest specific surface area (SSA) of 606 m²/g and 560 m²/g was noticed for UiO-66(Ce) obtained by hydrothermal synthesis on mixing M(1:1) and in sonochemical synthesis S(1:1), respectively. The material obtained via static hydrothermal synthesis H(1:1) was

characterized by significantly lower SSA. Hence, the motion of molecules in the solution, caused by stirring or ultrasounds, facilitated crystallization of structures having more developed surface than in the case of traditional, static hydrothermal synthesis. As was mentioned in the previous section, the agitation of solution during crystallization affects the nucleation and crystal growth; therefore, crystal size and size distribution must be determined. Stirring and sonication influence nucleation by shifting size distribution towards small particles and modifying the morphology of the obtained crystals, whereas the impact of ultrasounds is more important. In general, the UiO-66(Ce) materials obtained at M:L=2:1 had lower surface areas than those synthesized at M:L=1:1. However, the impact of metal: linker ratio was more pronounced for syntheses carried out under continuous stirring and in ultrasounds than in static hydrothermal synthesis. The lowest SSA (111 m²/g) was noticed for the M(2:1) sample that contained unwanted cerium formate, as was proven by the XRD (Figure 1).

The shapes of N₂ adsorption-desorption isotherms (Figure 4) of obtained materials are similar and reveal both adsorption at low relative pressures assigned to micropore filling, and adsorption at high relative pressures, which corresponds to N₂ adsorption in the interparticle voids.

The parent UiO-66(Zr) contains tetrahedral and octahedral cages of 0.8 nm and 1.1 nm width, respectively [41], and is microporous. The experiments of CO₂ sorption at 298 K showed that UiO-66(Ce) materials obtained in this work contain both micro- and mesopores (Table 2). In most of the samples, the volume fraction of micropores was predominant. It can be seen in Table 2 and Figure 5a that synthesis method affected pore size distribution for the samples obtained at M:L=1:1, i.e., the UiO-66(Ce) obtained in static hydrothermal synthesis (H) had the highest fraction of micropores, whereas increasing contribution of mesopores was observed in the samples obtained under stirring (44%) and sonication (67%). Combining the results of XRD (Table 1) with CO₂ sorption (Table 2), it can be noticed that the content of mesopores in the sample increased with decreasing crystallite size. For example, UiO-66(Ce) obtained in sonochemical synthesis was characterized by the smallest crystallite size and highest fraction of mesopores. It is very likely that the crystallites of UiO-66(Ce) generate mesoporous interparticle voids that are more numerous when smaller crystals are randomly packed. Moreover, the decrease in crystallite size should lead to a decrease of the internal surface area and increase of the external surface area, accompanied by a decrease in micropore volume [42].

Table 2. Pore volume, mean mesopores dimension, and fraction of micro- and mesopores in UiO-66(Ce) materials determined from CO₂ and benzene sorption (slit-pore model).

	S _{BET} [m ² /g]	V _{mic} +V _{mes} [cm ³ /g]	d _{mes} [nm]	Ø _{mic}	Ø _{mes}
H(1:1)	391	0.1810	4.37	0.84	0.16
M(1:1)	606	0.3079	7.94	0.56	0.44
S(1:1)	560	0.3120	10.42	0.33	0.67
H(2:1)	360	0.1970	5.98	0.70	0.30
M(2:1)	111	0.0679	5.42	0.78	0.22
S(2:1)	381	0.1860	7.99	0.66	0.34
UiO-66	1187 [6]				
	1086 [9]				
	1290 [41]				
	1080 [43]				
UiO-66(Ce)	1282 [12]				

Samples obtained at M:L=2:1, especially H(2:1) and S(2:1), are characterized with similar contribution of micro- and mesopores. Those two samples also had similar SSA, but they significantly differed in terms of crystallite size (Table 1). Syntheses carried out with the deficiency of organic linker are more likely to yield products with a higher concentration of structure defects, among which the most probable to occur are linker vacancy, i.e., microporous intraparticle void. Thus, for UiO-66(Ce) samples obtained at M:L=2:1, the fraction of micropores predominated over mesopore interparticle voids (thanks to the higher concentration of linker defects), regardless of the crystallite size.

UiO-66(Ce) materials reported in this work have significantly lower surface areas than other Zr and Ce based UiO-66 structures reported in the literature. This might be due to a considerably larger scale of synthesis than compared to [6,9,12,41], which also influenced the porosity of UiO-66(Ce) reported in this paper.

2.3. XPS of UiO-66(Ce)

Determination of cerium content and contribution of its oxidized and reduced state can be performed by using XPS, which is a surface sensitive technique that probes the top 10–12 nm of a film. It allows quantitative analysis of particular elements in the sample, including their oxidation state. The analysis of Ce3d photoemission spectra in Ce³⁺ and Ce⁴⁺ containing samples is not straightforward because it is composed of 10 peaks corresponding to both oxidation states. In addition, sample sputtering with Ar⁺ can cause reduction of some Ce⁴⁺ owing to loss of the lighter component, such as oxygen [44]. Thus, the artificial increase of the Ce³⁺ concentration can be observed. Nevertheless, it was found that the shorter the time of Ar⁺ sputtering, the lower is the degree of Ce reduction [45,46]. UiO-66(Ce) samples studied in this work were not subjected to Ar sputtering; hence any Ce³⁺ presence is not from oxygen scavenging. Figure 6 shows the Ce3d spectra for all synthesized UiO-66(Ce) samples, excluding M(2:1). In the ideal UiO-66 structure, the concentration of cerium is 5.55 at%, but in presented samples, it ranged from 6.07 to 7.19 at.%. Higher Ce concentration arises from the presence of linker vacancies. All spectra reveal 10 peaks that can be assigned to Ce³⁺ and Ce⁴⁺ cations, proving the presence of redox-active cerium atoms in the framework. The concentrations of particular cerium cations were similar, but Ce⁴⁺ predominated. In the ideal UiO-66 structure, cerium will exclusively occur in Ce⁴⁺. The presence of Ce³⁺ cations may be due to the occurrence of such structural defects as linker vacancies. As was presented in Figure 6, the synthesis method affected the contribution of Ce³⁺ cations, both in samples obtained at M:L=1:1 and M:L=2:1. In each group, the highest contribution of Ce³⁺ was noticed for samples obtained in static hydrothermal synthesis (H), and it slightly decreased when the synthesis was carried out under stirring (M) and ultrasounds (S). The presence of both oxidation states of cerium is important for the catalytic and adsorptive properties of UiO-66(Ce). Nonetheless, the detailed features of such a structure containing both Ce⁴⁺ and Ce³⁺ cations in the nodes have not been determined yet. However, it is known that under ambient conditions, both Ce(III) and Ce(IV) are stable valence states. Recently, Smolders et al. [15] published the outcome of their study on the redox behavior of cerium-based UiO-66 during oxidation of benzyl alcohol in the presence of TEMPO ((2,2,6,6-Tetramethylpiperidin-1-yl)oxyl). In the initial UiO-66(Ce), cerium was in its oxidized (Ce⁴⁺) state. Based on the Extended X-Ray Absorption Fine Structure (EXAFS), the authors reported that Ce⁴⁺ can be reduced to Ce³⁺ upon reaction conditions, perpetuating the structural integrity of the material. It was also found that larger ionic radii of Ce³⁺ (1.02 vs. 0.92 for Ce⁴⁺) led to a distortion in Ce cluster; thus, two different Ce-Ce distances occurred.

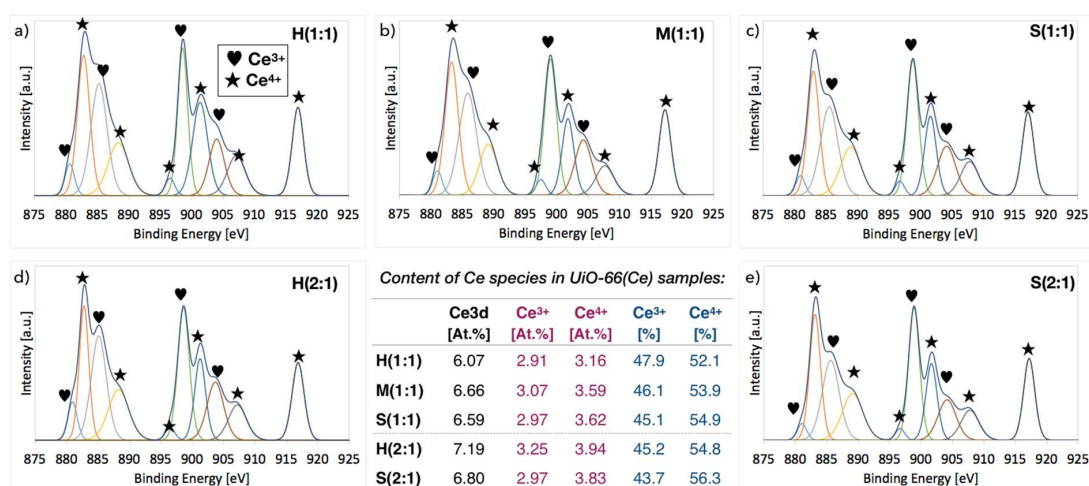


Figure 6. XPS Ce3d spectra and composition of UiO-66(Ce) samples.

2.4. Structure defects and thermal stability of UiO-66(Ce)

TGA-DTG was performed in order to learn about (i) thermal stability of each sample, (ii) the temperature that is needed to remove DMF from its pores and (iii) to determine the number of linker molecules attached to one Ce cluster. The UiO-66 structure is known to be very stable upon thermal treatment (up to 450 °C) [6]. However, the replacement of Zr ions to Ce resulted in a decrease of UiO-66 thermal stability, which was observed both in this work and reported elsewhere [12].

The TG and DTG curves for UiO-66(Ce) materials obtained at M:L=1:1 and 2:1 using three different synthesis methods are presented in Figure 7. According to TGA, all obtained structures are thermally stable up to ca. 260–280 °C (Table 3). The stability of UiO-66(Ce) up to 240 °C was proved by temperature-dependent PXRD—as reported by Lammert et al. [12]. Observed in Figure 7, weight loss at ca. 100 °C is due to moisture evaporation from the sample. The DMF evaporates at 156 °C; hence, the lack of weight loss at this temperature proves that solvent exchange after synthesis (DMF to chloroform) in the pores of UiO-66(Ce) was completed. However, it is quite possible that during synthesis, some DMF molecules formed an adduct with Ce precursor and were not exchanged with the BDC linker. Such a strongly coordinated to cerium cation DMF may be removed from the sample at a higher temperature. In the case of all UiO-66(Ce) samples (except for M(2:1)), some weight loss, that can be attributed to degradation of strongly coordinated DMF, was observed at ca. 240 °C. The XPS analysis showed that those samples contained from 1.2 at.% to 6.5 at.% of nitrogen (Table 3), proving the same DMF presence. Coordination of DMF to cerium cations was more important for materials obtained in syntheses, carried out under continuous stirring (M) and ultrasounds (S). Therefore, agitation of solution during synthesis helped DMF coordination to Ce clusters. In addition, linker deficiency in the mixture (M:L=2:1) also facilitates DMF attachment to cerium cluster.

Table 3. The average amount of BDC and DMF molecules coordinated to one Ce cluster in UiO-66(Ce).

Sample	Molecules per Ce Cluster			N [At.%] (from XPS)
	BDC	DMF	BDC+DMF	
H(1:1)	11.1	0.0	11.1	1.2
M(1:1)	10.2	1.2	11.4	2.1
S(1:1)	10.8	0.8	11.7	4.1
H(2:1)	9.8	0.4	10.2	1.4
M(2:1)	10.3	0.0	10.3	-
S(2:1)	9.1	2.4	11.5	6.5

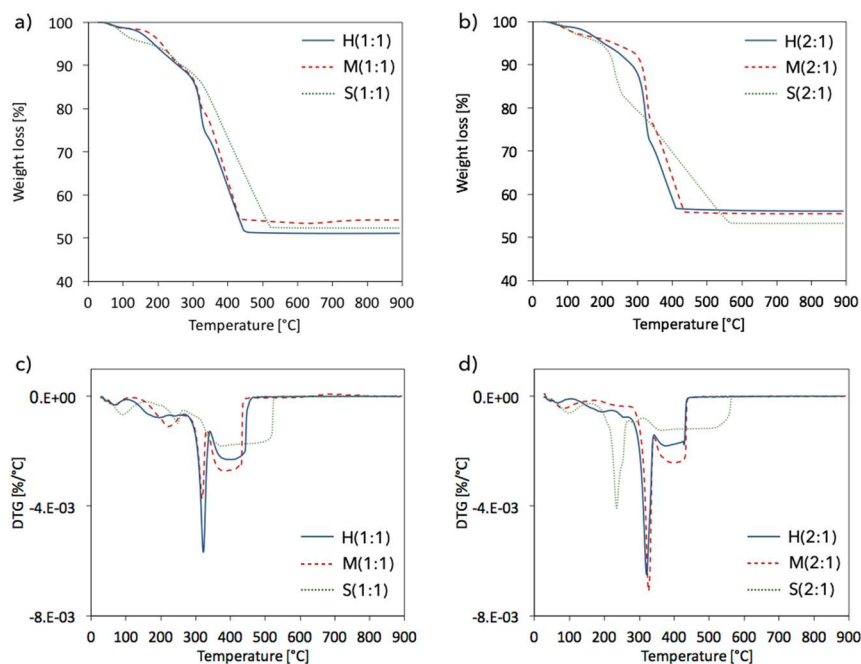


Figure 7. TG (a,b) and DTG (c,d) profiles for UiO-66(Ce) synthesized at M:L=1:1 (a,c) and M:L=2:1 (b,d).

Thermal decomposition of BDC linker in the obtained UiO-66(Ce) materials starts at ca. 260 °C and is followed by complete decomposition of the framework. Oxidation of BDC is completed at ca. 470 °C for the samples obtained in hydrothermal syntheses (H and M), and above 520 °C for samples obtained via the sonochemical method (S). Thermal decomposition of all samples leads to CeO₂. The DTG plots of samples obtained in hydrothermal syntheses (H and M) show that there are two weight loss regions above 260 °C: (i) sharp, negative peaks at ca. 320 °C, corresponding to 10–16% weight loss (depending on the sample), that can be attributed to degradation of terminal (surface) linker molecules, which have one unoccupied carboxylic group; therefore, are less stable thermally, and (ii) broad peaks at higher temperatures, corresponding to 15–25% weight loss, that can be assigned to degradation of more thermally resistant BDC that is connected to two Ce clusters. Hence, we may expect that surfaces of samples obtained in hydrothermal syntheses (H and M) are terminated with cerium clusters and BDC. The DTG profiles for samples obtained in sonochemical syntheses do not show peak at ca. 320 °C; therefore, those materials are probably terminated on their surfaces with cerium clusters.

The weight loss from 260 °C corresponds to the percentage of BDC in particular UiO-66(Ce) sample. In a defect-free UiO-66(Ce) structure, each Ce₆O₄(OH)₄ cluster coordinates 12 ligand molecules, which corresponds to 46.25% weight loss on TGA. For UiO-66(Ce) samples obtained in this work, the weight loss in the 260–600 °C range was lower, indicating the presence of structural defects due to missing linker molecules. It was reported [33,47] that removing some BDC linkers from UiO-66 yields a stable framework. According to our calculations (done based on Katz et al. [48]), one inorganic Ce₆O₄(OH)₄ cluster coordinated average from 9.8 to 11.1 BDC ligands (Table 3). This number of BDC ligands was affected by the synthesis method and applied M:L ratio. As was discussed above, in some of the samples, DMF coordinated with Ce clusters, occupying the place of BDC linker. More linker vacancies were noticed for samples synthesized with the excess of Ce precursor (the M(2:1) is not taken into consideration owing to the presence of cerium formate).

As was proven by XRD and TGA, linker vacancies are present in all UiO-66(Ce) samples. On one hand, missing linker means lower thermal stability of the structure, but on the other hand, it can positively influence the catalytic properties of MOF because defected (Figure 8b) or open metal sites (Figure 8c) are the adsorption sites for reagents. The removal of one BDC molecule from the original UiO-66 structure affects four Zr clusters and results in a reduction of its coordination from 12 to 11. The overall charge of such a defected structure is +2. In order to ensure charge neutrality, the dangling

bonds of the positively charged metal cluster may be saturated, e.g., with OH^- groups, anions of the acidic modulator (if used during synthesis) [49,50], or neutral molecules such as H_2O or DMF. Basically, linker removal is promoted by acidic modulators [51]; however, even if the synthesis is carried out without those modulators (like in this paper), the UiO-66 can have linker defects [50]. Linker vacancies in UiO-66 introduce coordinatively unsaturated Zr atoms, which results in open Lewis acid sites that is important for the adsorptive and catalytic properties of that material [52–54]. In the case of cerium-based UiO-66, the formation of linker vacancy may result either in lower valent cerium, i.e., Ce(III), or that vacancy may be compensated by $-\text{OH}$, H_2O or DMF, preserving the Ce(IV) and introducing Brønsted acid sites. The concentration of structural defects as well as the chemistry of defective metal cluster, either hydrated as shown in Figure 8b or dehydrated as displayed in Figure 8c, has an impact on the catalytic activity of MOF. For example, Caratelli et al. [55] reported that the activity of UiO-66 in esterification of levulinic acid with ethanol was higher for MOF having more linker defects and when the defective cluster was hydrated.

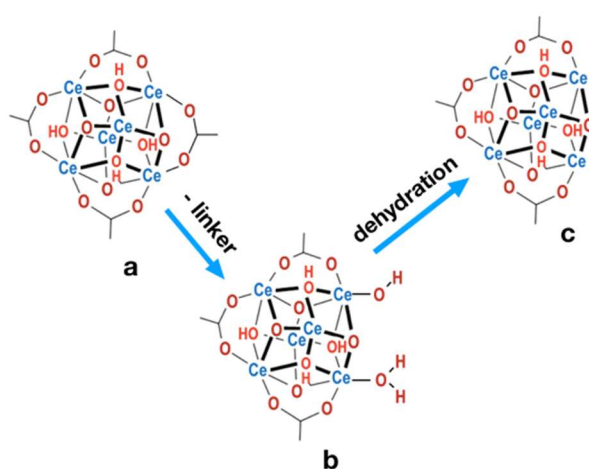


Figure 8. Ce cluster in UiO-66: defect-free 12-coordinated (a) and defective (after removal of 1 linker molecule) 11-coordinated, hydrated (b) and dehydrated (c).

According to TGA (Figure 7), the less-defected Ce sites were present in S(1:1) and S(2:1), where an average of 11.5 and 11.7 BDC+DMF molecules coordinated to one cerium cluster, respectively. In addition, as was shown in Figure 9, increasing concentration of linker vacancies (i.e., a decrease of the average number of BDC and BDC+DMF coordinated to one Ce cluster) went together with the increasing content of Ce^{3+} cations.

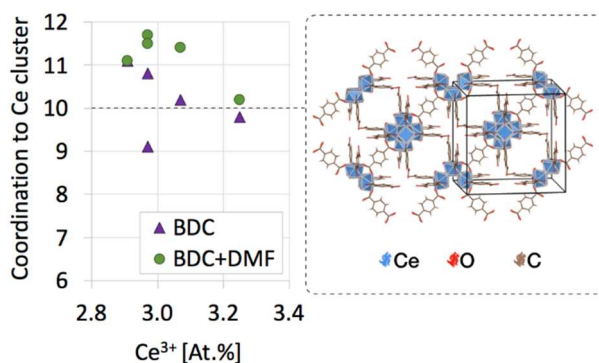


Figure 9. Coordination of BDC linker and DMF to one Ce cluster in UiO-66(Ce) vs. concentration of Ce^{3+} . On the right, the exemplary UiO-66(Ce) structure with linker vacancies corresponding to the average coordination of 10 linker molecules to one Ce cluster.

2.5. CO₂ adsorption on UiO-66(Ce)

The CO₂ adsorption on UiO-66(Ce) samples obtained by different methods was performed at 273 K and 298 K (Table 4). Higher CO₂ adsorptions were noticed for materials synthesized at M:L=1:1. In general, the amounts of CO₂ adsorbed in both temperatures varied significantly and were differently depended on factors such as specific surface area of the sample, content of Ce³⁺ and Ce⁴⁺ ions or concentration of structural defects caused by the missing linker (Figure 10.). It was found that CO₂ adsorption on UiO-66(Ce) samples at 273 K was not influenced by their SSA (Figure 10a), whereas it increased with Ce³⁺ content (Figure 10b). In contrary, CO₂ adsorption at 298 K increased with SSA of the sample, but did not depend on the Ce³⁺ contribution. It is known that carbon dioxide can adsorb both Ce³⁺ and Ce⁴⁺ ions, but it bounds more strongly to Ce³⁺. According to our research, CO₂ adsorption on reduced cerium cations in UiO-66(Ce) is favored only at low temperature (273 K).

Table 4. CO₂ adsorption and contribution of reversible and irreversible CO₂ adsorption on UiO-66(Ce) samples.

Sample	CO ₂ Adsorption at 273 K		CO ₂ Adsorption at 298 K	
	[mmol/g]	[mmol/g]	Reversible [%]	Irreversible [%]
H(1:1)	1.90	0.7640	83.6	16.4
H(2:1)	1.34	0.6125	84.6	15.4
M(1:1)	1.68	0.9011	92.9	7.1
M(2:1)	-	0.4328	58.5	41.5
S(1:1)	0.83	0.7545	74.9	25.1
S(2:1)	0.47	0.7498	75.1	24.9
CeO ₂	-	0.6528	47.8	52.2

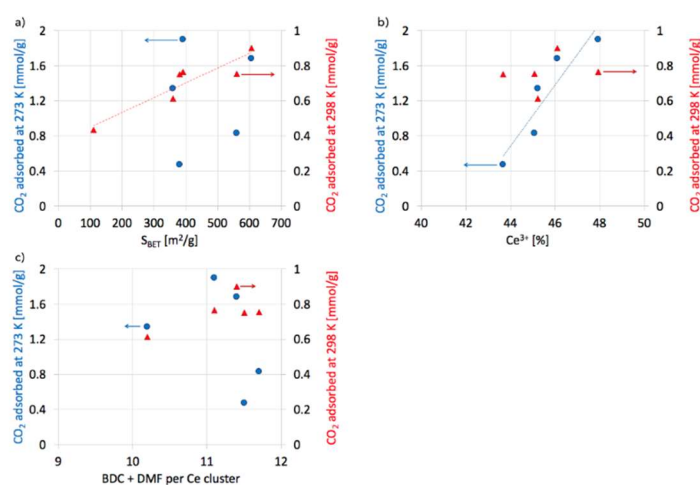


Figure 10. CO₂ adsorption at 273 K (●) and 298 K (▲) as a function of specific surface area (a), Ce⁴⁺ / Ce³⁺ ratio (b) and missing linker defect concentration (c) in the obtained UiO-66(Ce) materials.

The CO₂ adsorption-desorption tests carried out at 298 K revealed that some of CO₂ adsorbed on MOFs irreversibly (i.e., did not desorb entirely under vacuum at 298 K). To our best knowledge, the irreversible CO₂ adsorption on UiO-66(Zr) was reported only by Ethiraj et al. [56]. The contribution of reversible and irreversible CO₂ adsorption on UiO-66(Ce) samples is presented in Table 4. The M(2:1) sample was excluded from the discussion owing to the presence of cerium formate that probably transformed to cerium oxide upon heating under vacuum prior to CO₂ sorption. In that sample, the contribution of reversible and irreversible CO₂ adsorption was similar to nanocrystalline, commercial CeO₂ (Rhodia).

As was presented in Table 4, the synthesis method had a bigger impact on the amount of reversibly and irreversibly adsorbed CO₂ than the M:L ratio. The percentage of CO₂ that adsorbed irreversibly

on UiO-66(Ce) samples obtained by different methods decreased in the following order: S (~25%) > H (~16%) > M (~7%). Slightly higher contribution of irreversible CO₂ adsorption can be observed for samples synthesized at equimolar cerium to BDC ratio.

The CO₂ sorption capacities at 298 K are similar for H and S samples (Table 4) and somewhat higher for the M sample, which has the highest SSA. The concentration of cerium in all UiO-66(Ce) samples (calculated from XPS spectra) is also similar, but the concentration of Ce³⁺ ions, believed to be responsible for irreversible CO₂ adsorption, is the lowest for the materials obtained in sonochemical synthesis (S(1:1) and S(2:1)) (Figure 6). These samples, therefore, reveal the highest contribution of irreversible CO₂ adsorption probably due to the termination of S(1:1) and S(2:1) surfaces with cerium clusters (as was indicated by TGA). The concentration of Ce³⁺ at the surface of those samples was higher than in samples obtained in methods H and M, allowing more CO₂ to strongly (irreversibly) bond with cerium. D'Amato et al. [57] speculate that accumulation of Ce³⁺ near the external surface of UiO-66(Ce) can be due to water oxidation occurring at the solid/liquid interface during synthesis. Good argument for that can be the fact that cerium ammonium nitrate (CAN) is a stoichiometric oxidant in iridium catalyzed H₂O oxidation ($4\text{Ce}^{4+} + 2\text{H}_2\text{O} \rightarrow 4\text{Ce}^{3+} + 4\text{H}^+ + \text{O}_2$) [58]. Moreover, in acidic aqueous media, Ce⁴⁺ is an oxidizing reagent in the reaction of H₂O oxidation over ruthenium complexes [59].

Another factor that was found to have an impact on CO₂ adsorption was the concentration of missing linker molecules in the UiO-66(Ce) structure (Figure 10c). The concentration of this kind of structural defects is presented as the number of molecules of BDC linker (and DMF molecules, as discussed in Section 2.4) coordinated to one Ce cluster. The presence of missing linker defects (as well as missing cluster defects) in UiO-66 is normal and does not influence the framework, but may lead to different mechanical, adsorptive, and catalytic properties of this material [33]. Wu et al. [60] reported that linker vacancies enhanced the porosity of UiO-66 and had profound effects on the CO₂ adsorption. Whereas Thornton et al. [61], who computationally studied the role of defects, their variation, and heterogeneity, found that CO₂ uptake at low pressures (up to 1 bar) decreased with defects concentration and at high pressures (up to 35 bar) increased with defect concentration. Moreover, large cavities and pore volumes formed in UiO-66 owing to missing linker molecules led to higher CO₂ uptake. In the case of UiO-66(Ce) samples discussed here (Figure 10c), CO₂ adsorption at 298 K was the highest for the structure containing approximately one missing linker per Ce cluster, i.e., H(1:1). A lower concentration of linker vacancies (higher average coordination of Ce cluster) resulted in a gradual decrease in CO₂ sorption, which is in line with [61] and can be explained by the lower concentration of Ce³⁺ ions in less-defective samples, as was presented in Figure 9.

3. Materials and Methods

3.1. Synthesis of UiO-66(Ce)

A series of cerium-based UiO-66 were synthesized via three methods: hydrothermal (denoted H), hydrothermal with mixing (denoted M) and sonochemical (denoted S) (Figure 11). The Ce precursor was cerium (IV) ammonium nitrate (NH₄)₂Ce(NO₃)₆ (CAN, Fluka, ≥99.9%) while benzene-1,4-dicarboxylic acid (H₂BDC, Sigma Aldrich, 98%) was used as an organic linker. For each method, two metal: linker molar ratios (M:L), i.e., 1:1 and 2:1, were applied.

The UiO-66(Ce) materials were obtained according to the following procedure: The (NH₄)₂Ce(NO₃)₆ (5 mmol) was dissolved in deionized water (10 mL), whereas H₂BDC was dissolved in dimethylformamide (DMF) (30 mL for M:L=1:1 or 15 mL for M:L=2:1). Next, both solutions were mixed and subjected to three different procedures according to three different synthesis methods, i.e.:

1. *Hydrothermal synthesis (H)*: The mixture of Ce precursor and linker was placed in a Teflon lined steel autoclave and heated up to 110 °C in a dryer. After 30 min, the autoclave was slowly cooled down to room temperature.

2. *Hydrothermal synthesis with continuous mixing (M)*: The reagents mixture was placed in a Teflon lined steel autoclave and heated up to 110 °C in an oil bath that was placed on a magnetic stirrer. After 30 min, the autoclave was slowly cooled down to room temperature. The mixture was stirred throughout the whole synthesis, including heating and cooling steps.
3. *Sonochemical synthesis (S)*: The mixture of Ce precursor and linker was placed in a glass vessel and heated up to 50 °C in an ultrasound bath (35 kHz). After 30 min, the mixture was cooled down to room temperature.

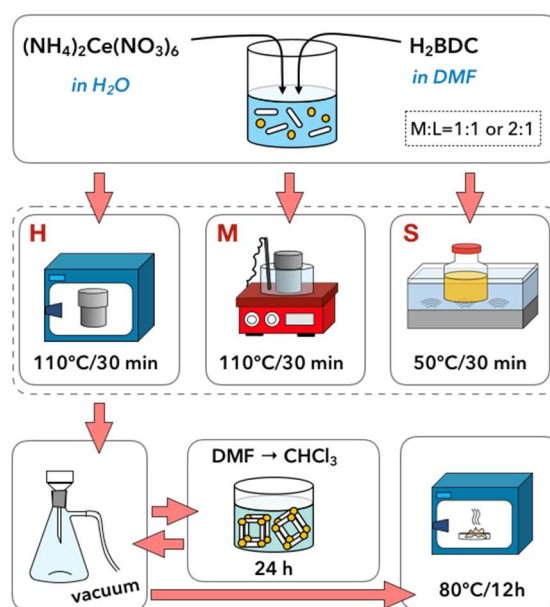


Figure 11. Scheme of the syntheses of UiO-66(Ce).

Obtained products were filtered off under vacuum and washed with H₂O and DMF in order to remove unreacted inorganic and organic substrates. In the next step, the DMF molecules were removed from UiO-66(Ce) pores and exchanged to chloroform (CHCl₃, Sigma Aldrich, ≥99.9%). The UiO-66(Ce) products were dispersed in 40 mL of CHCl₃, left for 24 h, and filtered off. This procedure was repeated three times. Finally, obtained powders were dried at 80 °C for 12 h. Synthesized UiO-66(Ce) materials were denoted X(M:L), where X is the method of synthesis (X= H, M or S) and M:L is the metal: linker molar ratio, i.e., 1:1 or 2:1. The yields of particular products were as follows: H(1:1)-50.9%, H(2:1)-46.0%, M(1:1)-49.3%, M(2:1)-45.2%, S(1:1)-43.5% and S(2:1)-40.0%.

3.2. Characterization of UiO-66(Ce)

In order to determine the textural properties, structure, morphology and thermal stability, the UiO-66(Ce) materials were characterized using various techniques and methods, including N₂, CO₂, and benzene adsorption/desorption, X-ray diffraction (XRD). Scanning electron microscopy (SEM), X-ray photoelectron spectroscopy (XPS) and thermogravimetric analysis (TGA).

The N₂ adsorption experiments were carried out on Autosorb 1C apparatus (Quantachrome Instruments) at 77 K. Prior to the measurements, the samples were outgassed in vacuum at 100 °C for 12 h. Specific surface areas were determined by the multipoint BET method. Specific total pore volume was evaluated from N₂ uptake at a relative pressure of P/P₀ = 0.99.

The porous structure of obtained UiO-66(Ce) was determined by CO₂ and benzene adsorption/desorption at 298 K. The CO₂ adsorption/desorption isotherms were obtained at a pressure ranging from 0 mmHg to 700 mmHg. Application of the Dubinin-Radushkiewicz (DR) equation allowed to determine the volume of micro- and mesopores accessible for CO₂. Moreover, the amount of reversibly and irreversibly adsorbed CO₂ was determined. Benzene adsorption/desorption isotherms (BET)

were obtained at a relative pressure P/P_0 ranging from 0 to 1. The desorption curve was used for determining the distribution of the volume and surface of slit type mesopores as a function of their dimension. Preceding CO_2 and benzene adsorption, the sample was degassed in vacuum at $100\text{ }^\circ\text{C}$. The CO_2 sorption capacity was also determined at 273 K, at relative pressure ranging from 0 to 1 bar. Prior to the measurement, the sample was degassed at $100\text{ }^\circ\text{C}$ for 12 h.

The powder XRD analyses were conducted using X'Pert Pro apparatus (PANalytical) using Ni-filtered Cu $K\alpha$ radiation ($\lambda = 1.54056\text{ \AA}$) equipped with specific optics to perform analysis by Small-angle X-Ray scattering (SAXS) in transmission geometry) with X'Pert HighScore Plus program used for display and analysis of the diffraction patterns. The scanning was performed from 5° to 80° with a rate of $0.03^\circ/\text{step}$.

The X-ray photoelectron spectroscopy (XPS) of the catalyst was performed using a Thermo-Scientific K-ALPHA spectrometer equipped in Al-K radiation (1486.6 eV) monochromatized by a twin crystal monochromator, yielding a focused X-ray spot with a diameter of $400\text{ }\mu\text{m}$, at $3\text{ mA} \times 12\text{ kV}$ when charge compensation was achieved with the system flood gun that provides low energy electrons and low energy argon ions from a single source. The hemispherical analyzer was operated in the constant energy mode with survey scan pass energies of 200 eV to measure the whole energy band, and 50 eV in a narrow scan to selectively measure particular elements. An estimation of the intensities was done after a calculation of each peak integral. S-shaped background subtraction and fitting of the experimental curve to a combination of a Lorentzian (30%) and Gaussian (70%) lines was done. Binding energies, referenced to the C1s line at 284.6 eV , had an accuracy of $\pm 0.1\text{ eV}$.

The thermogravimetric analysis (TGA) of the catalyst was performed using Mettler-Toledo apparatus. The change of sample mass was registered both in flowing air at a temperature increasing from $25\text{ }^\circ\text{C}$ to $900\text{ }^\circ\text{C}$ with a $10\text{ }^\circ\text{C}/\text{min}$ heating rate.

Scanning electron microscopy (SEM) analyses were carried out on a Jeol JSM-6610LVnx integrated with energy dispersive detector (EDS; Oxford Aztec Energy) unit with accelerating voltage ranging from 300 V to 300 kV .

4. Conclusions

A series of UiO-66(Ce) metal-organic frameworks were obtained by using three methods: static hydrothermal, hydrothermal under continuous stirring and (for the first time) sonochemical. The obtained samples were characterized for their composition, structure, morphology, textural properties, thermal stability, presence of structural defects, and CO_2 adsorption capacity.

It was found that the synthesis method affected the physicochemical properties of UiO-66(Ce). The agitation of the reaction mixture during synthesis (stirring or sonication) facilitated the formation of more developed surfaces and led to the formation of smaller crystallites of UiO-66(Ce) than when the synthesis was carried out in static conditions. All samples contained structural defects (coming from missing H_2BDC linker) that resulted in the presence of a lower valent cerium. It was found that the contribution of Ce^{3+} was linked to the concentration of linker vacancies (more defects = more Ce^{3+}). However, the charge on the defective Ce cluster was partly compensated, either by H_2O or DMF. As was determined by TGA, the coordination of DMF to Ce clusters was enhanced when synthesis was carried out under stirring or ultrasounds. The CO_2 sorption capacity at 273 K was the lowest for samples obtained by the sonochemical synthesis, and it increased with Ce^{3+} concentration. The CO_2 sorption on UiO-66(Ce) was found to take place in reversible as well as irreversible ways. The synthesis method significantly influenced the contribution of a particular type of adsorption; however, the important factor was not the concentration of Ce^{3+} ions (sites for strong CO_2 adsorption) but the termination of the surface sample with Ce clusters. High contribution of irreversible CO_2 adsorption was noticed for UiO-66(Ce) obtained using the sonochemical method. This method led to MOF having the smallest particles, which, in addition, were terminated with Ce clusters; therefore, the amount of Ce^{3+} accessible for strong CO_2 adsorption was higher than in the UiO-66(Ce) samples obtained by other methods and terminated, both with metal clusters and linker molecules.

In this work, we have shown that all of the used methods led to UiO-66(Ce) frameworks containing redox-active cerium atoms in the nodes (i.e., Ce⁴⁺ and Ce³⁺ cations), providing both Brønsted and Lewis acid centers, whose presence is important for MOF's performance in a given reaction. By using different synthesis methods, we can cause an impact on the character of active sites, textural properties, or even surface chemistry of MOF. Considering unique properties of cerium and excellent performance in many reactions, its introduction to metal nodes in Zr-based MOFs is an interesting area of research. The syntheses presented in this work were conducted on a scale ten times higher than those already reported [6,9,12,41] and will be improved in order to enhance UiO-66(Ce) properties, principally the size of the surface area. Moreover, the obtained UiO-66(Ce) will be tested in CO₂ hydrogenation to methanol.

Author Contributions: Conceptualization, A.Ł.; Data curation, M.S.; Formal analysis, M.S., R.Ł. and A.Ł.; Funding acquisition, M.S. and J.T.; Investigation, M.S., M.R., E.S., J.S.-A., M.Z., M.M., R.Ł., J.K. and A.Ł.; Methodology, A.Ł.; Resources, M.S., J.S.-A., M.Z., M.M. and J.K.; Supervision, A.Ł.; Validation, M.S. and A.Ł.; Visualization, A.Ł.; Writing—original draft, A.Ł.; Writing—review & editing, J.T. and A.Ł.

Acknowledgments: This work was financed by a statutory activity subsidy from the Polish Ministry of Science and Higher Education for the Faculty of Chemistry of Wrocław University of Technology and Project No 0402/0100/17.

Conflicts of Interest: The authors declare no conflict of interest.

References

1. Hong, D.H.; Suh, M.P. Selective CO₂ adsorption in a metal–organic framework constructed from an organic ligand with flexible joints. *Chem. Commun.* **2012**, *48*, 9168–9170. [[CrossRef](#)] [[PubMed](#)]
2. Liu, D.; Wu, H.; Wang, S.; Xie, Z.; Li, J.; Lin, W. A high connectivity metal–organic framework with exceptional hydrogen and methane uptake capacities. *Chem. Sci.* **2012**, *3*, 3032–3037. [[CrossRef](#)]
3. Nagarkar, S.S.; Joarder, B.; Chaudhari, A.K.; Mukherjee, S.; Ghosh, S.K. Highly selective detection of nitro explosives by a luminescent metal-organic framework. *Angew. Chem. Int. Ed.* **2013**, *52*, 2881–2885. [[CrossRef](#)]
4. Rojas, S.; Wheatley, P.S.; Quartapelle-Procopio, E.; Gil, B.; Marszalek, B.; Morris, R.E.; Barea, E. Metal-organic frameworks as potential multi-carriers of drugs. *CrystEngComm* **2013**, *15*, 9364–9367. [[CrossRef](#)]
5. Horike, S.; Dincă, M.; Tamaki, K.; Long, J.R. Size-Selective Lewis Acid Catalysis in a Microporous Metal-Organic Framework with Exposed Mn²⁺ Coordination Sites. *J. Am. Chem. Soc.* **2008**, *130*, 5854–5855. [[CrossRef](#)] [[PubMed](#)]
6. Hafizovic Cavka, J.; Jakobsen, S.; Olsbye, U.; Guillou, N.; Lamberti, C.; Bordiga, S.; Lillerud, K.P. A New Zirconium Inorganic Building Brick Forming Metal Organic Frameworks with Exceptional Stability. *J. Am. Chem. Soc.* **2008**, *130*, 13850–13851. [[CrossRef](#)]
7. Wang, B.; Yang, Q.; Guo, C.; Sun, Y.X.; Xie, L.H.; Li, J.R. Stable Zr(IV)-Based Metal-Organic Frameworks with Predesigned Functionalized Ligands for Highly Selective Detection of Fe(III) Ions in Water. *ACS Appl. Mater. Interfaces* **2017**, *9*, 10286–10295. [[CrossRef](#)]
8. Hafizovic Cavka, J.; Grande, C.A.; Mondino, G.; Blom, R. High Pressure Adsorption of CO₂ and CH₄ on Zr-MOFs. *Ind. Eng. Chem. Res.* **2014**, *53*, 15500–15507. [[CrossRef](#)]
9. Biswas, S.; Van Der Voort, P. A General Strategy for the Synthesis of Functionalised UiO-66 Frameworks: Characterisation, Stability and CO₂ Adsorption Properties. *Eur. J. Inorg. Chem.* **2013**, *2013*, 2154–2160. [[CrossRef](#)]
10. Jakobsen, S.; Gianolio, D.; Wragg, D.S.; Nilsen, M.H.; Emerich, H.; Bordiga, S.; Lamberti, C.; Olsbye, U.; Tilset, M.; Lillerud, K.P. Structural determination of a highly stable metal-organic framework with possible application to interim radioactive waste scavenging: Hf-UiO-66. *Phys. Rev. B Condens. Matter Mater. Phys.* **2012**, *86*, 125429–125439. [[CrossRef](#)]
11. Smith, S.J.D.; Ladewig, B.P.; Hill, A.J.; Lau, C.H.; Hill, M.R. Post-synthetic Ti Exchanged UiO-66 Metal-Organic Frameworks that Deliver Exceptional Gas Permeability in Mixed Matrix Membranes. *Sci. Rep.* **2015**, *5*, 7823. [[CrossRef](#)]
12. Lammert, M.; Wharmby, M.T.; Smolders, S.; Bueken, B.; Lieb, A.; Lomachenko, K.A.; Vos, D.D.; Stock, N. Cerium-based metal organic frameworks with UiO-66 architecture. *Chem. Commun.* **2015**, *51*, 12578–12581. [[CrossRef](#)]

13. Lammert, M.; Glißmann, C.; Reinsch, H.; Stock, N. Synthesis and Characterization of New Ce(IV)-MOFs Exhibiting Various Framework Topologies. *Cryst. Growth Des.* **2017**, *17*, 1125–1131. [[CrossRef](#)]
14. Dalapati, R.; Sakthivel, B.; Dhakshinamoorthy, A.; Buragohain, A.; Bhunia, A.; Janiak, C.; Biswas, S. A highly stable dimethyl-functionalized Ce(IV)-based UiO-66 metal-organic framework material for gas sorption and redox catalysis. *CrystEngComm* **2016**, *18*, 7855–7864. [[CrossRef](#)]
15. Smolders, S.; Lomachenko, K.A.; Bueken, B.; Struyf, A.; Bugaev, A.L.; Atzori, C.; Stock, N.; Lamberti, C.; Roeyfaers, M.B.J.; De Vos, D.E. Unravelling the redox-catalytic behavior of Ce⁴⁺-MOFs: A XAS study. *ChemPhysChem* **2018**, *19*, 373–378. [[CrossRef](#)]
16. Nouar, F.; Breeze, M.; Campo, B.C.; Clet, G.; Daturi, M.; Devic, T.; Vimont, A.; Walton, R.I.; Serre, C. Tuning the properties of the UiO-66 metal organic framework by Ce substitution. *Chem. Commun.* **2015**, *4*, 14458–14461. [[CrossRef](#)]
17. Sridharan, V.; Menéndez, J.C. Cerium(IV) Ammonium Nitrate as a Catalyst in Organic Synthesis. *Chem. Rev.* **2010**, *110*, 3805–3849. [[CrossRef](#)] [[PubMed](#)]
18. Esch, F.; Fabris, S.; Zhou, L.; Montini, T.; Africh, C.; Fornasiero, P.; Comelli, G.; Rosei, R. Electron localization determines defect formation on ceria substrates. *Science* **2005**, *309*, 752–755. [[CrossRef](#)]
19. Campbell, C.T.; Peden, C.H.F. Chemistry. Oxygen vacancies and catalysis on ceria surfaces. *Science* **2005**, *309*, 713–714. [[CrossRef](#)]
20. Li, Y.; He, X.; Yin, J.; Ma, Y.; Zhang, P.; Li, J.; Ding, Y.; Zhang, J.; Zhao, Y.; Chai, Z.; et al. Acquired superoxide-scavenging ability of ceria nanoparticles. *Angew. Chem. Int. Ed.* **2015**, *54*, 1832–1835. [[CrossRef](#)] [[PubMed](#)]
21. Wang, F.; Li, C.; Zhang, X.; Wei, M.; Evans, D.G.; Duan, X. Catalytic behavior of supported Ru nanoparticles on the {100}, {110}, and {111} facet of CeO₂. *J. Catal.* **2015**, *329*, 177–186. [[CrossRef](#)]
22. Trovarelli, A. Catalytic Properties of Ceria and CeO₂-Containing Materials. *Catal. Rev.* **1996**, *38*, 439–520. [[CrossRef](#)]
23. Graciani, J.; Mudiyansele, K.; Xu, F.; Baber, A.E.; Evans, J.; Senanayake, S.D.; Stacchiola, D.J.; Liu, P.; Hrbek, J.; Sanz, J.F.; et al. Catalysis. Highly active copper-ceria and copper-ceria-titania catalysts for methanol synthesis from CO₂. *Science* **2014**, *345*, 546–550. [[CrossRef](#)] [[PubMed](#)]
24. Wang, F.; Wei, M.; Evans, D.G.; Duan, X. CeO₂-based heterogeneous catalysts toward catalytic conversion of CO₂. *J. Mater. Chem. A* **2016**, *4*, 5773–5783. [[CrossRef](#)]
25. Jadhav, S.G.; Vaidya, P.D.; Bhanage, B.M.; Joshi, J.B. Catalytic carbon dioxide hydrogenation to methanol: A review of recent studies. *Chem. Eng. Res. Des.* **2014**, *92*, 2557–2567. [[CrossRef](#)]
26. Bonura, G.; Arena, F.; Mezzatesta, G.; Cannilla, C.; Spadaro, L.; Frusteri, F. Role of the ceria promoter and carrier on the functionality of Cu-based catalysts in the CO₂-to-methanol hydrogenation reaction. *Catal. Today* **2011**, *171*, 251–256. [[CrossRef](#)]
27. Arena, F.; Mezzatesta, G.; Zafarana, G.; Trunfio, G.; Frusteri, F.; Spadaro, L. Effects of oxide carriers on surface functionality and process performance of the Cu-ZnO system in the synthesis of methanol via CO₂ hydrogenation. *J. Catal.* **2013**, *300*, 141–151. [[CrossRef](#)]
28. Demessence, A.; D’Alessandro, D.M.; Foo, M.L.; Long, J.R. Strong CO₂ Binding in a Water-Stable. Triazolate-Bridged Metal-Organic Framework Functionalized with Ethylenediamine. *J. Am. Chem. Soc.* **2009**, *131*, 8784–8786. [[CrossRef](#)] [[PubMed](#)]
29. Lee, Y.R.; Kim, J.; Ahn, W.S. Synthesis of metal-organic frameworks: A mini review. *Korean J. Chem. Eng.* **2013**, *30*, 1667–1680. [[CrossRef](#)]
30. Kim, S.N.; Lee, Y.R.; Hong, S.H.; Jang, M.S.; Ahn, W.S. Pilot-scale synthesis of a zirconium-benzenedicarboxylate UiO-66 for CO₂ adsorption and catalysis. *Catal. Today* **2015**, *245*, 54–60. [[CrossRef](#)]
31. Safarifar, V.; Morsali, A. Applications of ultrasound to the synthesis of nanoscale metal-organic coordination polymers. *Coord. Chem. Rev.* **2015**, *292*, 1–14. [[CrossRef](#)]
32. Waitschat, S.; Fröhlich, D.; Reinsch, H.; Terraschke, H.; Lomachenko, K.A.; Lamberti, C.; Kummer, H.; Helling, T.; Baumgartner, M.; Henninger, S.; et al. Synthesis of M-UiO-66 (M = Zr, Ce or Hf) employing 2,5-pyridinedicarboxylic acid as linker: Defect chemistry, framework hydrophilisation and sorption properties. *Dalton Trans.* **2018**, *47*, 1062–1070. [[CrossRef](#)] [[PubMed](#)]
33. Øien, S.; Wragg, D.; Reinsch, H.; Svelle, S.; Bordiga, S.; Lamberti, C.; Lillerud, K.P. Detailed structure analysis of atomic positions and defects in zirconium metal-organic frameworks. *Cryst. Growth Des.* **2014**, *14*, 5370–5372. [[CrossRef](#)]

34. Shannon, R. Revised effective ionic radii and systematic studies of interatomic distances in halides and chalcogenides. *Acta Cryst. Sect. A* **1976**, *32*, 751–767. [[CrossRef](#)]
35. Henning, C.; Ikeda-Ohno, A.; Kraus, W.; Weiss, S.; Pattison, P.; Emerich, H.; Abdala, P.M.; Scheinost, A. Crystal structure and solution species of Ce(III) and Ce(IV) formates—from mononuclear to hexanuclear complexes. *Inorg. Chem.* **2013**, *52*, 11734–11743. [[CrossRef](#)] [[PubMed](#)]
36. Cordeiro, J.M.M.; Freitas, L. Study of Water and Dimethylformamide Interaction by Computer Simulation. *Z. Nat. A* **1999**, *54*, 110–116. [[CrossRef](#)]
37. García-Ruiz, J.M.; Otálora, F.; García-Caballero, A. The role of mass transport in protein crystallization. *Acta Cryst. F Struct. Biol. Commun.* **2016**, *72*, 96–104. [[CrossRef](#)] [[PubMed](#)]
38. Davey, R.J.; Schroeder, S.L.; Horst, J.H. Nucleation of organic crystals—a molecular perspective. *Angew. Chem. Int. Ed. Engl.* **2013**, *52*, 2166–2179. [[CrossRef](#)]
39. Dodds, J.A.; Espitalier, F.; Louisnard, O.; Grossier, R.; David, R.; Hassoun, M.; Baillon, F.; Gatamel, C.; Lyczko, N. The effect of ultrasound on crystallisation-precipitation processes: Some examples and a new segregation model. *Particle and Particle Systems Characterization. Part. Part. Syst. Charact.* **2007**, *24*, 18–28. [[CrossRef](#)]
40. Enomoto, N.; Sung, T.H.; Nakagawa, Z.E.; Lee, S.C. Effect of ultrasonic waves on crystallization from a supersaturated solution of alum. *J. Mater. Sci.* **1992**, *27*, 5239–5243. [[CrossRef](#)]
41. Furukawa, H.; Gándara, F.; Zhang, Y.B.; Jiang, J.; Queen, W.L.; Hudson, M.R.; Yaghi, O.M. Water Adsorption in Porous Metal-Organic Frameworks and Related Materials. *J. Am. Chem. Soc.* **2014**, *136*, 4369–4381. [[CrossRef](#)]
42. Aguado, J.; Serrano, D.P.; Escola, J.M.; Rodríguez, J.M. Low temperature synthesis and properties of ZSM-5 aggregates formed by ultra-small nanocrystals. *Microporous Mesoporous Mater.* **2004**, *75*, 41–49. [[CrossRef](#)]
43. De Coste, J.B.; Peterson, G.W.; Jasuja, H.; Glover, T.G.; Huang, Y.; Walton, K.S. Stability and degradation mechanisms of metal-organic frameworks containing the $Zr_6O_4(OH)_4$ secondary building unit. *J. Mater. Chem. A* **2013**, *1*, 5642–5650. [[CrossRef](#)]
44. Mitchell, D.F.; Sproule, G.I.; Graham, M.J. Sputter reduction of oxides by ion bombardment during Auger depth profile analysis. *Surf. Interface Anal.* **1990**, *15*, 487–497. [[CrossRef](#)]
45. Holgado, J.P.; Alvarez, R.; Munuera, G. Study of CeO XPS spectra by factor analysis: Reduction of CeO₂. *Appl. Surf. Sci.* **2000**, *161*, 301–315. [[CrossRef](#)]
46. Hattori, T.; Hattori, M.; Ozawa, M. Preparation and Surface Reduction Behavior of CeO₂ Nanoparticle Layer on Al₂O₃(0001) Crystal Substrate. *J. Surf. Sci. Nanotechnol.* **2018**, *16*, 172–176. [[CrossRef](#)]
47. De Vos, A.; Hendrickx, K.; Van Der Voort, P.; Van Speybroeck, V.; Lejaeghere, K. Missing Linkers: An Alternative Pathway to UiO-66 Electronic Structure Engineering. *Chem. Mater.* **2017**, *29*, 3006–3019. [[CrossRef](#)]
48. Katz, M.J.; Brown, Z.J.; Colón, Y.J.; Siu, P.W.; Scheidt, K.A.; Snurr, R.Q.; Hupp, J.T.; Farha, O.K. A facile synthesis of UiO-66. UiO-67 and their derivatives. *Chem. Commun.* **2013**, *49*, 9449–9451. [[CrossRef](#)] [[PubMed](#)]
49. Valenzano, L.; Civalieri, B.; Chavan, S.; Bordiga, S.; Nilsen, M.H.; Jakobsen, S.; Lillerud, K.P.; Lamberti, C. Disclosing the Complex Structure of UiO-66 Metal Organic Framework: A Synergic Combination of Experiment and Theory. *Chem. Mater.* **2011**, *23*, 1700–1718. [[CrossRef](#)]
50. Bristow, J.K.; Svane, K.L.; Tiana, D.; Skelton, J.M.; Gale, J.D.; Walsh, A. Free Energy of Ligand Removal in the Metal-Organic Framework UiO-66. *J. Phys. Chem. C* **2016**, *120*, 9276–9281. [[CrossRef](#)]
51. Vermoortele, F.; Bueken, B.; le Bars, G.; van de Voorde, B.; Vandichel, M.; Houthoofd, K.; Vimont, A.; Daturi, M.; Waroquier, M.; van Speybroeck, V. Synthesis Modulation as a Tool To Increase the Catalytic Activity of Metal-Organic Frameworks: The Unique Case of UiO-66 (Zr). *J. Am. Chem. Soc.* **2013**, *135*, 11465–11468. [[CrossRef](#)]
52. Fang, Z.; Bueken, B.; de Vos, D.E.; Fischer, R.A. Defect-Engineered Metal–Organic Frameworks. *Angew. Chem. Int. Ed. Engl.* **2015**, *54*, 7234–7254. [[CrossRef](#)]
53. Vermoortele, F.; Vandichel, M.; Van de Voorde, B.; Ameloot, R.; Waroquier, M.; VanSpeybroeck, V.; De Vos, D.E. Electronic Effects of Linker Substitution on Lewis Acid Catalysis with Metal-Organic Frameworks. *Angew. Chem. Int. Ed.* **2012**, *51*, 4887–4890. [[CrossRef](#)]
54. Cirujano, F.G.; Corma, A.; Llabrés i Xamena, F.X. Zirconium-containing metal organic frameworks as solid acid catalysts for the esterification of free fatty acids: Synthesis of biodiesel and other compounds of interest. *Catal. Today* **2015**, *257*, 213–220. [[CrossRef](#)]

55. Caratelli, C.; Hajek, J.; Cirujano, F.G.; Waroquier, M.; Llabrés i Xamena, F.X.; Van Speybroeck, V. Nature of active sites on UiO-66 and beneficial influence of water in the catalysis of Fischer esterification. *J. Catal.* **2017**, *352*, 401–414. [[CrossRef](#)]
56. Ethiraj, J.; Albanese, E.; Civalleri, B.; Vitillo, J.G.; Bonino, F.; Chavan, S.; Shearer, G.C.; Lillerud, K.P.; Bordiga, S. Carbon Dioxide Adsorption in Amine-Functionalized Mixed-Ligand Metal–Organic Frameworks of UiO-66 Topology. *ChemSusChem* **2014**, *7*, 3382–3388. [[CrossRef](#)]
57. D’Amato, R.; Donnadio, A.; Carta, M.; Sangregorio, C.; Vivani, R.; Taddei, M.; Costantino, F. Green Synthesis and Enhanced CO₂ Capture Performance of Perfluorinated Cerium-Based Metal–Organic Frameworks with UiO-66 and MIL-140 Topology. *ChemRxiv* **2018**. [[CrossRef](#)]
58. Bucci, A.; Menendez Rodriguez, G.; Bellachioma, G.; Zuccaccia, C.; Poater, A.; Cavallo, L.; Macchioni, A. An Alternative Reaction Pathway for Iridium Catalyzed Water Oxidation Driven by CAN. *ACS Catal.* **2016**, *6*, 4559–4563. [[CrossRef](#)]
59. Kimoto, A.; Yamauchi, K.; Yoshida, M.; Masaoka, S.; Sakai, K. Kinetics and DFT studies on water oxidation by Ce⁴⁺ catalyzed by [Ru(terpy)(bpy)(OH₂)₂]²⁺. *Chem. Commun.* **2012**, *48*, 239–241. [[CrossRef](#)]
60. Wu, H.; Shen Chua, Y.; Krungleviciute, V.; Tyagi, M.; Chen, P.; Yildirim, T.; Zhou, W. Unusual and Highly Tunable Missing-Linker Defects in Zirconium Metal–Organic Framework UiO-66 and Their Important Effects on Gas Adsorption. *J. Am. Chem. Soc.* **2013**, *135*, 10525–10532. [[CrossRef](#)]
61. Thornton, A.W.; Babarao, R.; Jain, A.; Trouseletc, F.; Coudert, F.X. Defects in metal–organic frameworks: A compromise between adsorption and stability. *Dalton Trans.* **2016**, *45*, 4352–4359. [[CrossRef](#)] [[PubMed](#)]



© 2019 by the authors. Licensee MDPI, Basel, Switzerland. This article is an open access article distributed under the terms and conditions of the Creative Commons Attribution (CC BY) license (<http://creativecommons.org/licenses/by/4.0/>).